

Carbonmonoxy Rebinding Kinetics in H93G Myoglobin: Separation of Proximal and Distal Side Effects

Stefan Franzen

Department of Chemistry, North Carolina State University, Raleigh, North Carolina 27695

Received: October 16, 2001; In Final Form: January 8, 2002

The kinetics of carbon monoxide (CO) recombination in H93G myoglobin has been studied as a function of temperature in aqueous buffer solution and in 75% glycerol/buffer solutions. H93G adducts with imidazole (Im), 4-methyl imidazole (4-Me Im), 1-methyl imidazole (1-Me Im), and 4-bromimidazole (4-Br Im) were analyzed by means of three-state and four-state sequential models. Rate constants for the inner process of CO forming a bond with iron and for CO ligand escape into the solvent were extracted from the analysis. At 310 K, where the largest differences are observed in buffer solution data, the rate constant for CO recombination to the heme iron differs by a factor of ≈ 15 for the various H93G proximal adducts, while the rate constant for CO escape differs by a factor of only ≈ 1.4 . Thermodynamic analysis based on microscopic reversibility shows that the effect of proximal adducts on equilibrium constant for the intrinsic CO binding to heme iron, K_{CO} , is 15 times larger than the effect on the equilibrium constant for ligand escape, K_{escape} . Arrhenius plots of the CO recombination rate constant yielded an average activation enthalpy of ≈ 17 kJ/mol for the rebinding rate constant for the CO recombination process in three of the adducts: Im, 1-Me Im, and 4-Br Im. A Landau–Zener model of the rate constant for the CO recombination process is introduced to account for differences observed in the prefactor of the rate constants. Combination of this analysis with potential energy surfaces calculated using the BLYP functional in a density functional theory approach with a large basis set indicates that the barrier to rebinding should be the same for the adducts studied in the absence of interaction with the protein. The origin of differences in activation enthalpy or entropy for substituted imidazole adducts of H93G therefore should arise from steric interactions with the protein.

Introduction

Heme proteins provide a fundamental means for testing the effect of solvent, or protein, structure on the kinetics of bond formation between a metal center and diatomic ligands. The enthalpic barrier to diatomic ligand recombination in photolyzed heme proteins is controlled by the coupling of the spin state of the heme iron to two structural coordinates. The first, or proximal, coordinate is the displacement of the metal center with respect to the heme plane. The second, or distal, coordinate consists of protein steric interactions with the diatomic ligand and the distance of the diatomic from the transition state. Mutants of myoglobin have provided important data for understanding the relative effects of these two factors on the barrier to geminate or cage rebinding since the trajectories of diatomic ligands (NO, CO, and O₂) are affected by the structure of protein around the heme iron.^{1–14} The majority of studies has focused on the steric effects of mutants in the distal pocket of myoglobin where photolyzed ligands reside (see Figure 1). Altering the size and polarity of distal residues affects ligand diffusion following flash photolysis. The nature of intrinsic or inner barrier to recombination to the heme iron can also be studied by systematically changing the proximal adduct trans to CO in proximal cavity mutants, such as the H93G mutant of myoglobin.^{15–19} In addition to the inner barrier to CO recombination, there is a barrier to CO escape into the solvent. At ambient temperatures, CO escape and caged CO recombination rate constants are sufficiently close to each other and a small change in either will have a substantial effect on the geminate yield for recombination.²⁰ Thus, it is important to design

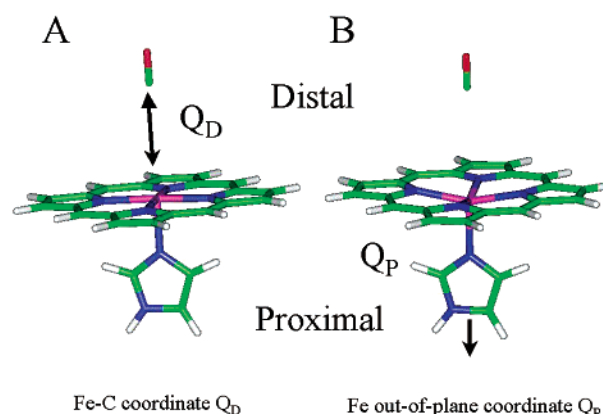


Figure 1. Illustration of an iron porphyrin CO model adduct. The iron–CO distance is a coordinate denoted Q_D . The iron out-of-plane coordinate is denoted Q_P . The distal side of the porphyrin ring is the site of CO ligation. The proximal side is the site of adduct formation with various nitrogenous molecules. (A) The iron is in the plane of the porphyrin ($Q_P = 0.0$ Å). (B) The iron is displaced 0.4 Å out of the heme plane ($Q_P = 0.4$ Å).

measurements that can separate CO recombination from CO escape to obtain measurements that determine the activation parameters. This study presents a set of data that show that such separation is possible and that the trans effect on activation parameters for CO recombination can be determined.

The iron in the heme cofactor of heme proteins has a number of functions including promoting catalysis in peroxidases and oxidases, initiating signaling in guanylate cyclase and CoxA,

and production of NO in NO synthase, to name a few.^{21–23} The globins are the easiest proteins to study to obtain a fundamental understanding of how ligand trajectories and the potential at the heme iron site both affect the overall kinetics and thermodynamics of ligand interactions with heme. However, the nature of the barrier and prefactor in an Arrhenius expression for the rate constant $k = A \exp\{-E_a/RT\}$ for CO recombination has been surprisingly difficult to characterize. The reason for this is that both proximal and distal factors can affect the kinetics of ligand rebinding.^{24–26} It is highly desirable to find a systematic procedure for separating the effects due to either protein or heme iron that can contribute to the observed kinetics. An explanation of the microscopic factors that govern diatomic ligand recombination will have general application to studies of ligand dynamics in heme proteins. Ligand dynamics, in turn, serve as a probe of protein dynamics that function to control signaling, transport, and enzymatic catalysis on the basis of binding events at the heme iron. Figure 1 shows an iron–porphine–CO model in both the bound and photolyzed forms. The iron–porphine adduct used for computation studies is an excellent model for the biologically relevant iron–porphyrin adducts. Porphine has the same aromatic ring and iron geometry as that found in iron–protoporphyrin IX or heme. In the following, the term heme will be used for discussion of experimental results in myoglobin mutants and the term porphine will be used to refer to the model calculations for the determination of the barrier to rebinding.

The present study addresses CO rebinding kinetics in the proximal cavity mutant of myoglobin, H93G, that permits substitution of the proximal adduct. In the H93G mutant, His93 that normally ligates the heme iron is substituted by glycine.^{16,17,27} This creates a cavity that can be filled with a variety of exogenous ligands that form adducts with the heme iron but are not covalently bound to the protein. The temperature dependence of CO rebinding kinetics was measured for four different proximal adducts in which the distal protein structure is essentially identical. The molecules studied were H93G(L)CO, where L is imidazole (Im); 4-methyl Im (4-Me Im); 4-bromo Im (4-Br Im); and 1-methyl Im (1-Me Im). In this series, the structure of the proximal adduct is largely conserved. X-ray crystal structures have been obtained for three of the adducts studied.^{15,18,19} Despite the structural similarities, the CO rebinding kinetics for these species are significantly different.¹⁷ The analysis presented here builds on previous studies of the effect of the proximal adducts on protein relaxation and binding affinities determined by measurement of association and dissociation rate constants.^{17,28}

The study of processes of CO recombination and escape must account for the fact that there is an inhomogeneous distribution of protein structures. Protein relaxation that occurs in myoglobin following ligand photolysis is a time-dependent manifestation of the inhomogeneity. Protein relaxation is observed in frequency shifts in Soret band, band III, or the time-resolved infrared spectra of the B states.^{3,28–36} The structural change that comprises protein relaxation may consist of a rearrangement around photolyzed CO in a docking site or a B site following ligand photolysis.^{28,37} An alternative hypothesis suggests that the spectral shifts arise from iron displacement and associated proximal conformational changes.^{30,31,36,38,39} The time scale and nature of the trapping of CO may affect recombination kinetics by affecting the attempt frequency for recombination with iron.³² The separation of protein relaxation and geminate recombination is difficult because protein relaxation is highly nonexponential, and thus even if the rapid phases are much more rapid than CO

recombination, there may be slow phases that occur on the time scale of CO recombination.^{29–31,40,41} In a previous study, it has been shown that the greatest part of protein relaxation measured by the time-dependent Soret band shift is more rapid than geminate recombination at temperatures above 250 K.^{28,42,43} However, complete separation of time scales is not possible and the observation of a static inhomogeneous distribution at ambient temperature in double-pulse experiments may arise from phases of protein relaxation that are slower than geminate recombination.^{29,40,41} The key point for the present study is that protein relaxation rates have been shown to be independent of the nature of proximal adducts in H93G.²⁸ Thus, by using the H93G(L)CO protein to compare the effect of various adducts, L, to the heme iron, the complexity introduced by protein relaxation can be neglected in the analysis of the CO recombination and escape rate constants.

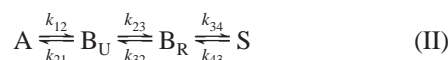
The fact that protein relaxation as monitored by the Soret band shift is not dependent on the nature of the iron adduct in H93G myoglobin suggests that H93G(L)CO is a good model system for the study of the inner barrier to CO recombination as distinct from protein relaxation and escape processes. The activation enthalpy of the intrinsic recombination process can be determined from Arrhenius plots. The prefactor can then be dissected into separate contributions. There is an *electronic contribution* due to nonadiabaticity that arises from the spin change from the S=2 spin configuration of the unligated iron to S=0 for iron bound to CO. There is a *distal conformational contribution* that consists of fluctuations in the distal pocket of the protein that may hinder the trajectory of the CO. There is a *proximal conformational contribution* that consists of the conformational changes required as the iron–imidazole adduct moves from the out-of-plane configuration of the deoxy form to the in-plane conformation of the CO form of the heme. The model presented here differs from a recent model⁴⁴ in a number of ways. A Landau–Zener (L–Z) approach⁴⁵ that is generally valid for CO, NO, and O₂ ligation is developed using the potential energy surfaces (PESs) calculated by density functional theory (DFT) as a starting point. The use of DFT to calculate the potential energy surface of heme model systems is well established.^{46–52} Experimental prefactors in both association and dissociation rate constants of myoglobin mutants have been shown to vary by orders of magnitude in some cases. In a L–Z approach, both the electronic coupling and the activation entropy can contribute to the magnitude of the prefactor. Entropic factors neglected in a previous model of the rate constant⁴⁴ are shown to depend on the geometry of the heme iron coordination sphere in the transition state. Previous experimental and theoretical work has shown that distal side protein motions hinder the CO trajectory along the reaction path by reducing the frequency factor for approach to the transition state.^{2–5,8,9,13,14,53} Recent studies of proximal mutants have shown that substantially smaller effects are observed.^{17,54,55} The experimental comparison of four different adducts L in H93G(L)CO provides an experimental approach that indicates that distal protein motions alone are not responsible for differences in the magnitude of Arrhenius prefactors. The approach developed here has validity for ligands other than CO and provides an experimental method for separating distal and proximal contributions to the intrinsic Fe–CO association rate constant.

Experimental Section

Transient absorption spectra were obtained using an apparatus and methodology described in detail elsewhere.³³ Analysis of time-dependent spectra was carried out using singular value

decomposition (SVD). The application of SVD to the kinetics of recombination in hemoglobin and myoglobin has been described in detail.^{33,35,56} In previous studies, SVD analysis of time-dependent spectra allowed the data to be represented as three dominant eigenvalues.²⁸ The corresponding components consist of one due primarily to ligand rebinding and two due largely to protein relaxations as probed by the Soret band shift. The separation of the band shift as an indicator of protein relaxation and of the kinetics for geminate recombination has been presented in earlier work.²⁸ In the present study, the kinetics for wild-type Sperm Whale myoglobin (SWMb) and for several ligand adducts L in the mutant H93G(L) are examined to understand the role played by the ligand in the inner barrier to CO recombination.

Methods for obtaining kinetic rate constants and barriers in the context of a three- or four-state sequential model for ligand binding have been developed in detail by several groups.^{3,20,57} For photolyzed myoglobin (Mb*CO), a sequential reaction scheme for three and four states can be written as



where A represents the ligand-bound form MbCO and B represents the ligand in the first of several possible potential energy minima between A and the solvent denoted S. For the three-state model, the intermediate state is denoted B. The state B is often denoted Mb:CO which indicates that the ligand is in the distal pocket adjacent to the heme iron and only the innermost barrier separates them. The intrinsic Fe—CO association process is k_{21} in both schemes. The observed geminate rate constant $k_{\text{geminate}} = k_{21} + k_{23}$ is the sum of the intrinsic association and escape rate constants. The schemes assume a static distribution of conformers and do not allow for protein relaxation.³⁵ The above models assume that averaging over equilibrium conformations is rapid compared to the fastest rate constant. This is not necessarily the case for photolyzed MbCO since there are two states A_0 , the open state, and A_1 , the closed state, whose interconversion appears sufficiently close to the geminate rate constant that there may be a conformational contribution.^{29,40,41}

Recent studies of NO and O₂ rebinding kinetics, time-dependent infrared measurements, and a time-dependent X-ray crystal structure have all suggested that there is either a branch point or a relaxation process that is required in the sequential model.^{8,58–63} A branch or relaxation in the kinetic model can arise, for example, from the presence of at least two conformations of CO in a docking site above the heme in photolyzed MbCO.³² A nonexponential relaxation of the type observed in time-dependent Soret band and band III peak shifts can arise because of an inhomogeneous distribution of relaxing myoglobin molecules each with a single-exponential relaxation rate constant.⁶⁴ The hypothesis of an inhomogeneous distribution supported by the observation that the relaxation can be solidified into an inhomogeneous distribution of structures either at low temperature^{29,36,38,39,58,62} or high-solvent viscosity.⁶⁵ The four-state model (eq II) used here is a sequential model that can also accommodate an inhomogeneous distribution as discussed elsewhere.⁶⁶

Data were obtained at ambient temperature in aqueous buffer solution in 75% glycerol/buffer glasses. The CO rebinding kinetics of H93G(L)CO in buffer solution in the temperature

region above 280 K are well fit by two exponentials. The analysis of biexponential kinetics in terms of geminate and bimolecular processes has been described previously. The observed geminate rate constant, $k_{\text{geminate}} = k_{23} + k_{21}$, is the sum of the inner barrier and escape rate constants. The geminate yield is $\Phi_{\text{geminate}} = k_{21}/(k_{23} + k_{21})$ and the observed bimolecular rate constant is $k_{\text{bimolecular}} = \Phi_{\text{geminate}} k_{32}$. The intrinsic rate constants k_{12} , k_{23} , and k_{32} can be obtained from the fits of solution data to a biexponential model $N(t) = A_1 \exp\{-k_1 t\} + A_2 \exp\{-k_2 t\}$, provided the decay is normalized so that $A_1 + A_2 = 1$, using the following relations: $\Phi_{\text{geminate}} = A_1$, $k_{21} = A_1 k_1$, $k_{23} = (1 - A_1) k_1$, $k_{32} = k_2/A_1$ (Table 4). The quantity $N(t)$ is the fraction of uncombined MbCO molecules following a photolysis flash, $N(t) = \Delta A(t)/\Delta A(0)$. Kinetic data in 75% glycerol/buffer glass show an increasing number of exponential phases as the temperature is lowered. These observations agree with many studies that have focused on the nonexponential CO rebinding kinetics of photolyzed MbCO in glycerol/buffer glasses and other viscous media both above and below the glass transition temperature. The kinetic fitting function employed here for data in 75% glycerol/buffer solutions is a stretched exponential for the most rapid phase of geminate CO recombination plus two exponential phases, $N(t) = A_1 \exp\{-(k_1 t)^\beta\} + A_2 \exp\{-k_2 t\} + A_3 \exp\{-k_3 t\}$ where β is the Kolrausch parameter.⁶⁷

Potential energy surfaces for both low spin ($S=0$) and high spin ($S=2$) manifolds of an iron—porphine—CO model were obtained by density functional theory (DFT) using both the generalized gradient approximation (GGA) of Perdew and Wang⁶⁸ and the BLYP functional^{69,70} as implemented in DMol3 (Molecular Simulations Inc.).^{71,72} All calculations were carried out on the SGI/Cray Origin 2000 and IBM SP supercomputers at the North Carolina Supercomputer Center (NCSC). Numerically tabulated basis sets of double- ζ plus polarization (DNP) and double- ζ plus extra polarization (DNPP) quality were employed as described in the Supporting Information. For the DNP basis, there are three basis functions for hydrogen (1s, 2s, 2p); six basis functions for first-row elements carbon, nitrogen, and oxygen (1s, 2s(2), 2p(2), 3d); and 10 basis functions for iron (1s, 2s, 2p, 3s, 3p, 3d(2), 4s(2), 4p). For the DNPP basis, there are four basis functions for H (1s, 2s, 2p, 3d); seven basis functions for C, N, and O (1s, 2s(2), 2p(2), 3d, 4f); and 12 basis function for iron (1s, 2s, 2p, 3s, 3p, 3d(2), 4s(2), 4p, 4f, 5g). The DNPP basis set was parametrized by Bartolotti.⁷³ For the iron—porphine adduct with imidazole and CO, the total number of DNP basis functions is 532 and the total number of DNPP basis functions is 851. The potential energy surfaces were tested for both Fermi (canonical ensemble)⁷⁴ and Thermal (grand canonical ensemble) treatments of the density functional wherever possible. However, in the course of calculating potential energy surfaces, the canonical ensemble sometimes fails to converge. Therefore, the reported surfaces are those using the grand canonical ensemble.⁷⁵ The grand canonical (Thermal) option always converged to a lower overall energy. The grand canonical calculations were carried out at a temperature of $k_B T = 0.02$ eV. Once the calculation is complete, it can be extrapolated to zero temperature by addition of the grand canonical partition function. The Fermi and Thermal surfaces agreed to within ≈ 3 kJ/mol when corrected for a constant offset (see Supporting Information). AVS (Advanced Visual System) and insightII (Molecular Simulations) programs were used for visualization of the results.

TABLE 1: Fit Parameters for a Fitting Model with Two Exponential Functions and One Stretched Exponential Applied to the 75% Glycerol/Buffer Kinetic Data Obtained at 290, 270, and 250 K

290 K	A_1	$k_1 (\times 10^{-6} \text{ s}^{-1})$	A_2	$k_2 (\times 10^{-5} \text{ s}^{-1})$	A_3	$k_3 (\times 10^{-2} \text{ s}^{-1})$	β
WT	0.073	3.74	0.079	5.49	0.859	7.30	1.0 ^a
4-Me	0.138	8.97	0.164	6.96	0.717	10.76	1.0 ^a
Im	0.157	10.85	0.187	7.55	0.675	12.89	1.0 ^a
1-Me	0.276	17.79	0.250	9.83	0.512	20.60	1.0 ^a
270 K	A_1	$k_1 (\times 10^{-7} \text{ s}^{-1})$	A_2	$k_2 (\times 10^{-5} \text{ s}^{-1})$	A_3	$k_3 (\times 10^{-2} \text{ s}^{-1})$	β
WT	0.311	0.222	0.105	5.20	0.583	3.61	0.420 ^b
4-Me	0.585	0.358	0.098	3.52	0.317	2.67	0.367
Im	0.653	0.669	0.088	6.85	0.260	5.08	0.360 ^b
1-Me	0.784	2.51	0.088	12.5	0.124	7.67	0.339
250 K	A_1	$k_1 (\times 10^{-7} \text{ s}^{-1})$	A_2	$k_2 (\times 10^{-4} \text{ s}^{-1})$	A_3	$k_3 (\times 10^{-2} \text{ s}^{-1})$	β
WT	0.821	0.0966	0.020	0.274	0.159	1.09	0.220 ^b
4-Me	0.939	1.39	0.018	0.198	0.042	0.47	0.222
Im	0.950	2.64	0.018	0.500	0.032	0.91	0.211
1-Me	0.957	17.1	0.030	3.93	0.013	2.36	0.239

^a Fixed value $\beta = 1.0$ gives the same result as the three-exponential fit discussed elsewhere. See reference 28. ^b Value was fixed to be similar to the β values for comparison sake.

TABLE 2: Sequential Kinetic Model with Four Intermediates Applied to 75% Glycerol/Buffer Data^a

290 K	$k_{21} (\times 10^{-6} \text{ s}^{-1})$	$k_{23} (\times 10^{-6} \text{ s}^{-1})$	$k_{32} (\times 10^{-5} \text{ s}^{-1})$	$k_{34} (\times 10^{-5} \text{ s}^{-1})$	$k_{43} (\times 10^{-6} \text{ M}^{-1} \text{ s}^{-1})$
WT	0.270	3.47	0.501	5.45	8.67
4-Me Im	1.21	7.76	1.54	6.75	5.78
Im	1.67	9.17	2.00	7.24	5.94
1-Me Im	4.73	13.1	4.25	8.70	6.28
270 K	$k_{21} (\times 10^{-6} \text{ s}^{-1})$	$k_{23} (\times 10^{-6} \text{ s}^{-1})$	$k_{32} (\times 10^{-5} \text{ s}^{-1})$	$k_{34} (\times 10^{-5} \text{ s}^{-1})$	$k_{43} (\times 10^{-6} \text{ M}^{-1} \text{ s}^{-1})$
WT	0.690	1.53	0.888	4.92	2.36
4-Me	2.10	1.48	0.922	2.98	1.13
Im	4.37	2.33	1.90	5.60	2.00
1-Me	19.7	5.42	5.61	8.13	1.88
250 K	$k_{21} (\times 10^{-7} \text{ s}^{-1})$	$k_{23} (\times 10^{-6} \text{ s}^{-1})$	$k_{32} (\times 10^{-4} \text{ s}^{-1})$	$k_{34} (\times 10^{-4} \text{ s}^{-1})$	$k_{43} (\times 10^{-6} \text{ M}^{-1} \text{ s}^{-1})$
WT	0.0793	0.173	0.0317	0.248	0.963
4-Me	1.31	0.837	0.0621	0.136	0.156
Im	2.51	1.31	0.185	0.324	0.251
1-Me	16.3	7.32	2.83	1.22	0.338

^a The analysis of the four-state model is described in detail elsewhere. See ref 3.

Results

Ligand Rebinding Kinetics in 75% Glycerol/Buffer Solution. The ligand rebinding progress curves for SWMbCO, H93G(Im)CO, H93G(1-Me Im)CO, and H93G(4-Me Im)CO at 250, 270, and 290 K have been reported elsewhere.²⁸ The differences in CO rebinding kinetics for different proximal ligands in the H93G mutant can be contrasted with the nearly identical Soret band shifts in these species discussed elsewhere.²⁸ The ligand rebinding kinetics of H93G(L)CO are faster than wild-type, and the geminate yields are larger. The order for rebinding rate (and geminate yield) at all temperatures is H93G-(1-Me Im)CO > H93G(Im)CO > H93G(4-Me Im)CO > SWMbCO. As indicated in Table 1, the magnitude of the Kolrausch parameter β in the stretched exponential fitting function decreases as the temperature decreases. For the data at 290 K, β was set equal to one since these data were well fit by a three exponential function as discussed in a previous study.²⁸ For 270 and 250 K data, the average values of β are $\beta \approx 0.36$ and $\beta \approx 0.22$, respectively, indicating a broader distribution of rate constants as the temperature is lowered. The rate constants and coefficients are given in Table 1. The magnitude of β in Table 1 was fixed for certain fits to maintain similar distribution widths at a given temperature for comparison sake. The residuals of the fits in which β was a free parameter showed no systematic features and represented only random

noise in the data. Where β was fixed, there was a small deviation in the residuals at short times.

The elementary rate constants for the four kinetic traces at 290 K are given in Table 2 on the basis of application of a four-state sequential model. At 290 K, a four-state sequential model can be applied, and all approximations hold rigorously.³ The rate constant for CO recombination to the heme iron from the inner barrier, k_{21} , is by far the most affected by substitution of different proximal ligands and is a factor ≈ 17.5 larger in H93G(1-Me Im)CO than in SWMbCO recombination. The escape rate constant, k_{34} , increases by a factor ≈ 1.6 and the bimolecular recombination rate constant, k_{43} , decreases by a factor ≈ 1.5 when the same species are compared. Application of the four-state model to the 270 and 250 K data can be carried out by assuming that the stretched exponential rate constant k_1 in Table 1 is an average rate constant for the geminate process.² It is not possible to deduce from the fits whether the non-exponential contribution is present in the CO recombination rate constant k_{inner} or the escape rate constant k_{escape} . If it is assumed that the rate constants k_{21} , k_{23} , and k_{32} are all part of the geminate process that includes protein relaxation, we can compare the escape rate constant k_{34} and bimolecular recombination rate constant k_{43} . At 250 K, the rate constants k_{34} and k_{43} change by factors of ≈ 9 and ≈ 6 , respectively, for the heme environments studied. Although these values are much larger than the change

TABLE 3: Biexponential Fits to Buffer Data near Ambient Temperature

275 K	A_1	$k_1 (\times 10^{-6} \text{ s}^{-1})$	A_2	$k_2 (\times 10^{-3} \text{ s}^{-1})$
4-Me Im	0.112	0.789	0.879	0.355
Im	0.186	0.917	0.802	0.690
4-Br Im	0.236	1.168	0.735	0.845
1-Me Im	0.334	1.492	0.633	1.714
280 K	A_1	$k_1 (\times 10^{-6} \text{ s}^{-1})$	A_2	$k_2 (\times 10^{-3} \text{ s}^{-1})$
4-Me Im	0.093	1.016	0.907	0.470
Im	0.158	1.259	0.842	0.932
4-Br Im	0.202	1.543	0.798	1.121
1-Me Im	0.302	2.026	0.698	2.376
290 K	A_1	$k_1 (\times 10^{-6} \text{ s}^{-1})$	A_2	$k_2 (\times 10^{-3} \text{ s}^{-1})$
4-Me Im	0.058	1.669	0.942	0.678
Im	0.103	2.224	0.896	1.421
4-Br Im	0.136	2.966	0.864	1.567
1-Me Im	0.214	3.872	0.786	3.627
300 K	A_1	$k_1 (\times 10^{-6} \text{ s}^{-1})$	A_2	$k_2 (\times 10^{-3} \text{ s}^{-1})$
4-Me Im	0.036	2.819	0.964	0.909
Im	0.066	3.633	0.934	1.863
4-Br Im	0.089	5.570	0.911	2.182
1-Me Im	0.150	6.660	0.850	4.824
310 K	A_1	$k_1 (\times 10^{-6} \text{ s}^{-1})$	A_2	$k_2 (\times 10^{-3} \text{ s}^{-1})$
4-Me Im	0.021	3.858	0.979	1.120
Im	0.042	6.621	0.958	2.353
4-Br Im	0.058	10.583	0.942	2.639
1-Me Im	0.102	12.358	0.898	6.327

at 290 K, they must be compared to an increase in the inner CO recombination rate by a factor of over 200 for the k_{21} process at 250 K (Table 2). There is some systematic error in the kinetic data at 250 K for the escape and bimolecular rates since the bimolecular yields are very small. Given the high viscosity of the medium at this temperature, there is likely an inhomogeneous distribution for the escape process as well as for the relaxation

processes in the protein. These issues have been treated in a recent study that applies to NO recombination and the problem of ligand escape when the bimolecular yield is very small.⁶⁶ Despite these complications, the overall result is that the dependence of the escape and bimolecular process is at least an order of magnitude less sensitive to the proximal ligand geometry than the inner process of CO recombination to the heme iron.

Comparison of Rebinding Kinetics in Buffer Solution. To address the question of whether the proximal ligand substitutions affect the dynamics of ligand rebinding on the distal side, kinetic measurements were performed on the CO rebinding for several ligands L in H93G(L)CO as a function of temperature in buffer solution. Biexponential fits to the data for the ligands 4-Me Im, Im, 4-Br Im, and 1-Me Im presented in Table 3 are readily analyzed using a three-state model to yield the elementary rate constants presented in Table 4. There is a significant dependence of the inner rate constant, k_{21} , and a much smaller dependence of ligand escape (k_{23}) and entry (k_{32}) rate constants, on the identity of the proximal ligand, L. For example, at 275 K the ratios of the most rapid reactions observed for H93G-(1-Me Im)CO to the slowest process observed for H93G(4-Me Im)CO are ≈ 5.6 , ≈ 1.4 , and ≈ 1.6 for k_{21} , k_{23} , and k_{32} , respectively. These trends are maintained for all of the temperatures studied with the ratio of k_{21} for any two species in Table 4 being 4–10 times larger than the corresponding ratio for k_{23} or k_{32} .

Density Functional Calculation of CO Ligand Rebinding. The potential energy surface for the Fe–CO bond was determined for both quintet and singlet spin states of four H93G adducts at three geometries. In Figure 1, the out-of-plane coordinate and the Fe–C bond length are defined as Q_P and Q_D , respectively. The geometries that correspond to the potential energy surfaces in Figure 2 consist of the iron in the heme plane, $Q_P = 0.0$ Å in Figure 2A, and displacements of the Fe–Im adduct by $Q_P = 0.2$ and $Q_P = 0.4$ Å out of the heme plane in

TABLE 4: Fit of Buffer Data at Four Temperatures to a Sequential Three-State Kinetic Model

275 K	$k_{21} (\times 10^{-5} \text{ s}^{-1})$	$k_{23} (\times 10^{-6} \text{ s}^{-1})$	$k_{32} (\times 10^{-6} \text{ M}^{-1} \text{ s}^{-1})$	$k_{23}/k_{32} (\times 10^{-5} \text{ M})$
4-Me Im	0.883	0.700	3.17	221
Im	1.71	0.746	3.71	201
4-Br Im	2.76	0.892	3.58	249
1-Me Im	4.98	0.994	5.13	193
280 K	$k_{21} (\times 10^{-5} \text{ s}^{-1})$	$k_{23} (\times 10^{-6} \text{ s}^{-1})$	$k_{32} (\times 10^{-6} \text{ M}^{-1} \text{ s}^{-1})$	$k_{23}/k_{32} (\times 10^{-5} \text{ M})$
4-Me Im	0.945	0.922	5.05	183
Im	1.99	1.060	5.90	180
4-Br Im	3.12	1.231	5.54	222
1-Me Im	6.12	1.414	7.87	180
290 K	$k_{21} (\times 10^{-5} \text{ s}^{-1})$	$k_{23} (\times 10^{-6} \text{ s}^{-1})$	$k_{32} (\times 10^{-6} \text{ M}^{-1} \text{ s}^{-1})$	$k_{23}/k_{32} (\times 10^{-5} \text{ M})$
4-Me Im	0.968	1.572	11.7	134
Im	2.29	1.995	13.8	145
4-Br Im	4.03	2.563	11.5	223
1-Me Im	8.29	3.043	16.9	180
300 K	$k_{21} (\times 10^{-5} \text{ s}^{-1})$	$k_{23} (\times 10^{-6} \text{ s}^{-1})$	$k_{32} (\times 10^{-6} \text{ M}^{-1} \text{ s}^{-1})$	$k_{23}/k_{32} (\times 10^{-5} \text{ M})$
4-Me Im	1.01	2.72	25.3	108
Im	2.40	3.39	28.2	120
4-Br Im	4.96	5.07	24.5	207
1-Me Im	9.99	5.66	32.2	176
310 K	$k_{21} (\times 10^{-5} \text{ s}^{-1})$	$k_{23} (\times 10^{-6} \text{ s}^{-1})$	$k_{32} (\times 10^{-6} \text{ M}^{-1} \text{ s}^{-1})$	$k_{23}/k_{32} (\times 10^{-5} \text{ M})$
4-Me Im	0.810	3.78	53.3	71
Im	2.78	6.34	56.0	113
4-Br Im	6.14	9.97	45.5	219
1-Me Im	12.6	11.1	62.0	179

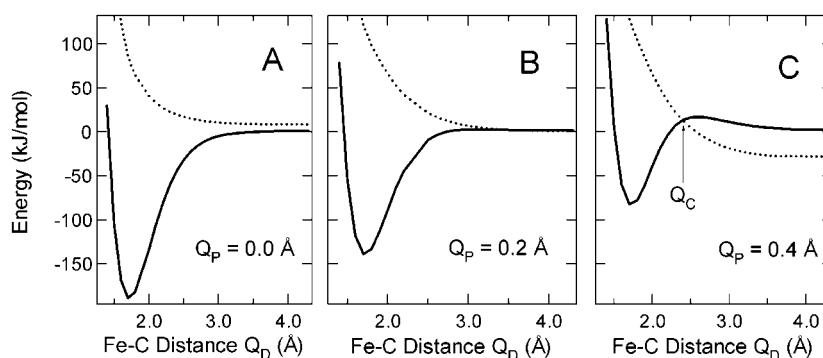


Figure 2. Potential energy surfaces for singlet (—) and quintet (···) states for various iron out-of-plane displacements. (A) The Fe–C distance Q_D is plotted for an in-plane iron ($Q_P = 0$ Å). (B) The Fe–C distance Q_D is plotted for iron displaced 0.2 Å out of the heme plane ($Q_P = 0.2$ Å). (C) The Fe–C distance Q_D is plotted at $Q_P = 0.4$ Å.

TABLE 5: Equilibrium Bond Lengths from Geometry Optimized Structures Using the GGA Functional and DNP Basis Set

species	Fe–N ϵ (Å)	Fe–N ρ (Å)	Fe–C (Å)	C–O (Å)
4-Me Im	2.049	2.018	1.781	1.158
Im	2.074	2.020	1.786	1.157
4-Br Im	2.058	2.020	1.788	1.157
1-Me Im	2.046	2.018	1.782	1.158

Figure 2B and C, respectively. The approach of using more than one coordinate to describe the potential surface is analogous to previous models^{38,53} that include an iron and protein coordinate in the description of rebinding and relaxation. The difference in the present approach is that the coordinates are distal Q_D and proximal Q_P that depend on the heme geometry alone. The model is designed to separate the innermost barrier from the protein coordinate.

To determine the critical factors that influence the barrier to rebinding, the relative energies of the spin manifolds must be correctly calculated. The spin gap $E_{\text{singlet}} - E_{\text{quintet}}$ and quintet state PES are well calculated by the DNPP basis set but not by the DNP basis set. The quintet manifold calculated for the DNP basis set indicates that there is a bound state for CO that has a binding energy of ≈ 58 kJ/mol and an Fe–C bond length of ≈ 2.0 Å. In this respect, the PESs calculated using the GGA functional with the DNP basis set are similar to those obtained using Gaussian94 and a 6-31G basis set, which also indicates that the quintet state is a bound state.⁴⁴ By contrast, the quintet state calculated using the DNPP basis set and BLYP functional is completely dissociative for the Fe–C bond in agreement with experiment. The singlet and quintet PESs are shown for three iron out-of-plane geometries in Figure 2, $Q_P = 0.0, 0.2$, and 0.4 Å. Furthermore, the spin gap in the DNPP calculation agrees with experiment since the quintet state is lower than the singlet state when $Q_P > 0.2$ Å. For these reasons, the DNPP calculation was used in the calculations shown in Figure 2 and for numerical comparisons made in this study. To reduce computation expense, the geometry-optimized structures using the DNP basis set were used as the reference geometry. The bond lengths for the optimum geometry are given in Table 5. The frequencies and energies for the DNP calculation have been shown to be in reasonable agreement with experiment.⁵²

In an effort to determine the origin of the barrier to rebinding, calculations were also carried out along Q_P , the Fe out-of-plane coordinate. Remarkably similar PESs were found for each of four proximal adducts, Im, 4-Br Im, 4-Me Im, and 1-Me Im, and therefore only the calculated PES corresponding to the imidazole adduct is shown. Quintet states, singlet states, and the spin gap between these states were essentially identical for

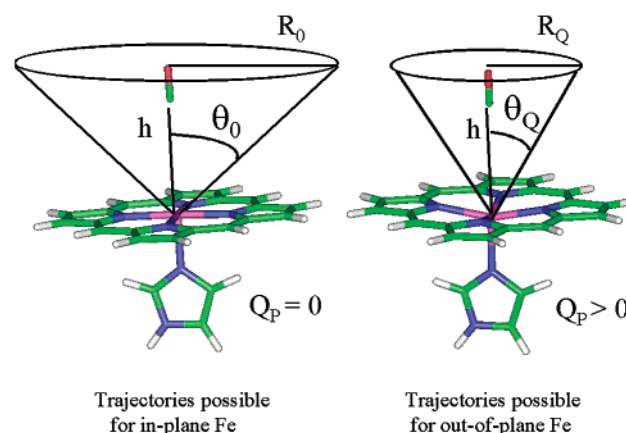


Figure 3. Illustration of the restriction on ligand trajectories for out-of-plane geometries relative to in-plane geometries. The access cones shown are for illustration purposes only. The volume accessible to the CO ligand in the transition state is given by $\pi h R^2/2$ where the radius R varies with Q_P for the out-of-plane distance because of steric interactions with the pyrrole nitrogens of the porphine.

all four adducts. The significance of the similarity of the calculated potential energy surfaces is that it strongly suggests that intrinsic electronic effects are not responsible for the differences in kinetics of CO recombination in H93G(L)CO.

The barrier to CO rebinding can be either along Q_P , since the iron must move into the heme plane to reduce the spin gap, or Q_D , since the CO ligand can recombine by a thermal process even if the spin gap is present. The barrier to rebinding along Q_D is ≈ 40 kJ/mol for an out-of-plane displacement of 0.4 Å. The barrier to motion of the iron into the heme plane Q_P is ≈ 20 kJ/mol as shown in Figure 4. However, since the spin gap (and hence the barrier along Q_D) vanishes by $Q_D \approx 0.2$ Å, the barrier to iron motion toward a possible transition state could be smaller than 20 kJ/mol. The location of the crossing point on the two-dimensional surface presented by the coordinates Q_P and Q_D likely depends on the protein environment that determines the additional energy cost of the proximal motion of iron along Q_P and CO along Q_D , respectively. In addition, as discussed below, the transition state will be determined by electronic and entropic terms as well.

The CO bond energy of ≈ 189 kJ/mol is nearly identical for the proximal adducts Im, 4-Me Im, 1-Me Im, and 4-Br Im regardless of the computation method employed. This result is consistent with a previous study in which major changes in electronic structure of the proximal imidazole (e.g., proton abstraction to create imidazolate) were shown to result in only a modest weakening of the Fe–C bond (≈ 12 kJ/mol).⁵² Thus, the DFT calculations show that ligand basicity does not affect

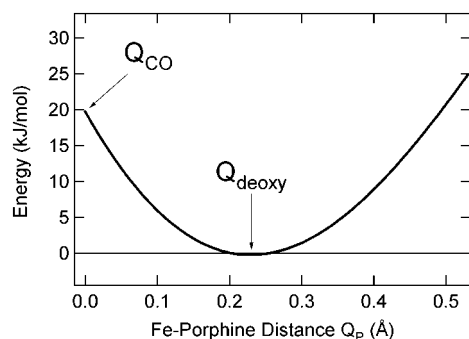


Figure 4. Plot of the energy surface for the Q_P distance for four adducts to iron carbonmonoxy porphine. The Q_P coordinate is relative to an in-plane iron geometry (shown in Figure 1A), for which $Q_P = 0.0$ Å. The calculated energies are based on a DFT calculation for iron out-of-plane displacement for each of the four adducts studied, H93G(Im), H93G(4-Me Im), H93G(1-Me Im), and H93G(4-Br Im). The result was almost identical for all four adducts and so a polynomial fit to the average is presented in the Figure.

the bond energy of CO for the substituted imidazole adducts of H93G considered here.

Discussion

Separation of Ligand Escape and Geminate Recombination Processes. Analysis of the kinetic data in Table 4 shows that it is primarily the rate constant for the inner barrier to recombination at the heme iron (k_{21}) that is affected by substitution of the axial adduct L in the adducts of H93G(L)CO studied here. There are three separate processes that involve the heme–protein complex in controlling diatomic ligand recombination. One can identify rate constants for a rapid relaxation process that ensues after photolysis, $k_{\text{relaxation}}$, ligand escape, k_{escape} , and an inner barrier process, k_{inner} . The competition between ligand escape and geminate rebinding determines the geminate yield Φ_{geminate} . In a three-state model, these quantities correspond as follows: $k_{\text{inner}} = k_{21}$ and $k_{\text{escape}} = k_{23}$. In a four-state model, the escape rate corresponds to the outer barrier, $k_{\text{escape}} = k_{34}$, with the rate constants k_{23} and k_{32} accounting for dynamics within the globin. Tables 2 and 4 show that k_{escape} (k_{23} or k_{34}) depends more strongly on temperature and viscosity than the inner process. This is immediately evident from the fact that geminate yield in SWMbCO in 75% glycerol/buffer solution is $\Phi_{\text{gem}} \approx 0.07$, which is nearly double that in buffer solution.²⁰ The bimolecular rate constants, $k_{\text{bimolecular}}$, are k_{32} and k_{43} in the three-state and four-state models, respectively. The results show that the dependence of k_{inner} on proximal adduct L is more than 1 order of magnitude greater than that of k_{escape} or $k_{\text{bimolecular}}$ in glycerol/buffer solution and a factor of 4–10 at all temperatures in aqueous buffer solution.

Temperature Dependence of the Rate Constants. The results of Arrhenius plots of k_{inner} and k_{escape} are given in Tables 6 and 7, respectively, on the basis of the kinetic data obtained in aqueous buffer solution (Table 3). The H93G(L)CO adducts L = 1-Me Im, 4-Br Im, and Im give relatively similar results for k_{inner} . The average activation enthalpy for these species is $\Delta H^\ddagger \approx 17$ kJ/mol (Table 6), somewhat larger than that observed in wild-type SWMb at ambient temperature. However, the 4-Me Im adduct has a substantially lower activation enthalpy and prefactor. The activation enthalpy for H93G(4-Me Im)CO is a factor of 5 lower than the average for the other adducts with a value of $\Delta H^\ddagger \approx 3.4$ kJ/mol. The prefactor is 3 orders of magnitude smaller for H93G(4-Me Im)CO than for the other proximal adducts. The k_{escape} and $k_{\text{bimolecular}}$ rate constants for

TABLE 6: Fit Parameters for Arrhenius Plot of the Rate Constant k_{21} for the Association of CO with the Heme Iron Obtained from the Data in Buffer Solution from 275 to 310 K

adduct	A	Ea (kJ/mol)	ΔS^\ddagger (J/mol·K) ^a	ΔH^\ddagger (kJ/mol)
4-Me Im	4.00×10^5	3.4	−137.6	3.4
Im	2.94×10^8	17.0	−82.8	17.0
4-Br Im	3.25×10^8	16.2	−81.9	16.2
1-Me Im	1.46×10^9	18.3	−69.5	18.3

^a The activation entropy calculated assumes a transition-state model with kT/h calculated at a temperature of 300 K.

TABLE 7: Fit Parameters for Arrhenius Plot of the Escape Rate Constant k_{23} Obtained from the Data in Buffer Solution from 275 to 310 K

adduct	A	Ea (kJ/mol)	ΔS^\ddagger (J/mol·K) ^a	ΔH^\ddagger (kJ/mol)
4-Me Im	7.28×10^6	−37.1	−113.5	−37.1
Im	9.80×10^7	−42.6	−91.4	−42.6
4-Br Im	1.78×10^{10}	−49.1	−67.3	−49.1
1-Me Im	1.78×10^{10}	−48.8	−67.3	−48.8

^a The activation entropy calculated assumes a transition-state model with kT/h calculated at a temperature of 300 K.

TABLE 8: Fit Parameters for Arrhenius Plot of the Bimolecular Rate Constant k_{32} Obtained from the Data in Buffer Solution from 275 to 310 K

adduct	A	Ea (kJ/mol)	ΔS^\ddagger (J/mol·K) ^a	ΔH^\ddagger (kJ/mol)
4-Me Im	2.15×10^{14}	−56.9	10.3	−56.9
Im	9.66×10^{13}	−54.8	3.63	−54.8
4-Br Im	2.16×10^{13}	−51.5	−8.83	−51.5
1-Me Im	1.77×10^{13}	−50.0	−10.5	−50.0

^a The activation entropy calculated assumes a transition-state model with kT/h calculated at a temperature of 300 K.

the four adducts studied in aqueous buffer solution have average activation enthalpies of $\Delta H^\ddagger \approx 44$ kJ/mol (Table 7) and $\Delta H^\ddagger \approx 53$ kJ/mol (Table 8), respectively. There is a systematic trend toward larger barriers for escape (Table 7) and smaller barriers for the bimolecular process (Table 8) in the order 4-Me Im, Im, 4-Br Im, 1-Me Im. It is interesting to compare these results with the temperature dependence of the equilibrium constants for the escape process given in column 5 of Table 4. The 1-Me Im and 4-Br Im adducts of H93G have CO escape equilibria that are nearly temperature independent, $K_{\text{escape}} = k_{23}/k_{32} \approx 1.80$ and 2.20×10^{-5} M, respectively. The escape equilibrium constants for the 4-Me Im and Im adducts decrease by a factor of 3 and 2, respectively, over the temperature range of 275–310 K. The equilibrium constant for CO rebinding, K_{CO} , can be determined using k_{off} data (k_{12} in eq I) according to the method developed in the Supporting Information. The intrinsic CO equilibrium constant for the process MbCO \rightarrow Mb:CO can be obtained either from a comparison of the off rates and on rates together with the escape rate constants, $K_{\text{CO}} = K_{\text{escape}}(k_{\text{on}}/k_{\text{off}})$, or from the ratio k_{21}/k_{12} . Using the data in ref 17 in Table 9, the K_{CO} equilibrium constant is compared for the two methods in columns 7 and 8, respectively. The comparison shows that reasonable agreement can be obtained and that the equilibrium constant for the CO binding event can be determined.

The prefactors in the Arrhenius equation are more variable for the inner CO process than for the escape or bimolecular process. The variation in the prefactor in H93G(L)CO comparisons for different proximal adducts cannot be explained by distal side chain motions. Instead, the data force consideration of the electronic and entropic factors that determine the inner CO rebinding rate constant.

TABLE 9: Comparison of k_{on} and k_{off} Data with the Flash Photolysis Data for the Calculation of K_{CO}

adduct	k_{off}^a or k_{12} ($\times 10^{-2}$ s $^{-1}$)	k_{21} ($\times 10^{-5}$ s $^{-1}$) ^b	k_{on}^a ($\times 10^{-6}$ M $^{-1}$ s $^{-1}$)	$k_{\text{on}}/k_{\text{off}}^a$ ($\times 10^{-6}$ M $^{-1}$)	k_{23}/k_{32}^b ($\times 10^{-5}$ M)	$k_{\text{on}}/k_{\text{off}}$ (k_{23}/k_{32})	k_{21}/k_{12}
4-Me Im	1.4	1.01	1.2	86	1.08	929	720
Im	1.2	2.40	1.7	141	1.20	1690	2000
4-Br Im	1.1	4.96	2.0	167	2.07	3460	4500
1-Me Im	0.77	9.99	4.3	558	1.76	9820	12970

^a From ref 17. ^b From Table 4 in this work.

Landau–Zener Model for Diatomic Ligand Rebinding.

The fit to an Arrhenius rate expression $k_{\text{inner}} = A \exp(-E_a/RT)$ can be expressed as a transition-state theory rate constant $k_{\text{TST}} = \eta \exp\{\Delta S^\ddagger(Q_P, Q_D)/R\} \exp\{-\Delta H^\ddagger(Q_P, Q_D)/RT\}$ where ΔS^\ddagger and ΔH^\ddagger are the activation entropy and enthalpy, respectively. The activation parameters are given in terms of the two coordinates Q_P and Q_D . The parameter η is a frequency factor that can be expressed in two alternative forms of the transition-state theory rate constant:

$$\eta = \frac{kT}{h} \quad \text{classical TST}$$

$$\eta = \frac{|H_{12}|^2 \omega \sqrt{2\pi M}}{\hbar \frac{d}{dQ}(H_{11} - H_{22}) \sqrt{kT}} \quad \text{Landau–Zener}$$

Here, ω is a frequency factor that indicates the number of times per second that the crossing point Q_c is traversed. M is the mass of the CO molecule. The Landau–Zener prefactor can be derived from P , the probability that a jump occurs from one potential surface to the other on a single passage through the transition state. The Landau–Zener transition probability is

$$P = \exp\left\{-\frac{2\pi H_{12}^2}{\hbar v \frac{d}{dQ}(H_{11} - H_{22})_{Q_c}}\right\}$$

In the above expression, v is the velocity of a collective nuclear coordinate as it passes through the transition state. The terms dH_{11}/dQ and dH_{22}/dQ represent the slope of the reactant and product states at the transition state. H_{12} is the electronic coupling between the reactant and product states at the transition state. The L–Z probability is a useful form for consideration of transitions in adiabatic and nonadiabatic limits. The application to the geminate recombination process in heme proteins is relevant since certain diatomic ligands (e.g., NO and O₂) appear to have extremely rapid phases of geminate recombination indicative of an adiabatic reaction, while CO geminate recombination is several orders of magnitude slower indicating a nonadiabatic process. The consideration of whether the crossing is adiabatic or nonadiabatic rests on the magnitude of H_{12} . H_{12} is equal in magnitude to twice the splitting in energy between the reactant surface (surface 1) and product surface (surface 2) at the crossing point Q_c (see Figure 2C). Since the coupling of singlet and quintet states involves change in spin, the nature of H_{12} involves time-dependent spin–orbit coupling or charge-transfer matrix elements that couple the two spin manifolds. It has been shown elsewhere that iron-ring charge transfer is the mechanism for photolysis.²⁶ The thermal recombination process may also involve charge transfer between the iron and diatomic ligand. Indeed, the Fe(III)O₂– resonance structure is thought to be important for equilibrium binding of O₂. The L–Z model provides a means to consider the factors that could influence the electronic contribution of various proximal ligands to the prefactor.

The similarity of the PESs and distal protein dynamics suggests that the electronic contribution to the prefactor A is the same for all of the proximal adducts. The lack of dependence of protein relaxation and ligand escape rates on the chemical identity of the proximal adduct indicates that the parameter v , the relative velocity of Fe and CO in the vicinity of the transition, is a constant for the proximal adducts considered here. The fact that the PESs as a function of Q_D are identical for the various proximal adducts (Figure 2) indicates further that H_{12} , dH_{11}/dQ , and dH_{22}/dQ are the same for all adducts. Hence, the dependence of the prefactor A on the identity of the ligand cannot be attributed to an electronic term and must arise from differences in the activation entropy (column 4 of Table 6). The comparison of 1-Me Im and 4-Me Im is particularly instructive since the pK_a values of these two molecules are similar (7.2 and 7.5, respectively),⁷⁶ and they have nearly identical conformations in the metaquo form of H93G as determined by X-ray crystallography.¹⁸ In summary, the electronic factor is not strongly affected by the proximal ligand.

Since the electronic frequency factor η is not responsible for the differences, the classical transition-state theory prefactor kT/h can be applied in the analysis of the kinetic data in Table 6 for the sake of comparison of H93G(L)CO for various L's. In this discussion, it is recognized that some part of the activation entropy calculated in Table 6 is due to a distal side conformational contribution to the prefactor as well.^{8,44} However, that contribution is common to all of the proximal adducts. Thus, the relative value of $\Delta\Delta S^\ddagger = \Delta S^\ddagger(L_2) - \Delta S^\ddagger(L_1)$ for two proximal adducts L_1 and L_2 depends mainly on Q_P , the iron out-of-plane displacement and any associated proximal conformations. The effects as a function of Q_P can be separated into (1) the effect that Q_P has on the partition function at the transition state because of changes in CO trajectories as a function of Q_P and (2) conformational effects specific to a particular adduct. Focusing on the first effect, the activation entropy ΔS^\ddagger should become more negative as Q_P increases because the possible angles of incidence for CO binding is decreased (translational effect) and the degrees of freedom available for rotation to reach the transition state are also reduced (rotational effect). The activation entropy is dictated by the available trajectories for the CO approach to the heme iron. In principle, the azimuthal angle of approach of the CO, θ shown in Figure 3, defines a conical volume for possible trajectories to the heme iron. This volume is larger for an in-plane heme iron than for an out-of-plane geometry ($Q_P > 0$). We can estimate the contribution to ΔS^\ddagger by considering the change in the available volume for CO trajectories as the angle grows smaller. Ignoring the geometry of amino acids in the distal pocket, we can assume that the available volume for recombination to in-plane heme iron is given by a hemisphere above the heme iron. Given that the volume of the access cone shown in Figure 3 is $V_j = \pi R_j^2 h/2$ and $R_j = \tan(\theta_j)$, The relative translational molar entropy is given by the $\Delta\Delta S^\ddagger = \Delta S_Q^\ddagger - \Delta S_0^\ddagger = R \ln\{\tan^2(\theta_{Q_P})/\tan^2(\theta_0)\}$ where the angles θ refer to the maximum possible declination angle for CO in a recombination trajectory as shown in Figure 3. For example, if we assume

that θ_0 is 60° and θ_Q is 20° , then $\Delta\Delta S^\ddagger \approx -26 \text{ J/mol}\cdot\text{K}$ for an out-of-plane iron compared to an in-plane iron. Restricted rotation can have an even larger effect on the activation entropy. If rotation to the transition state is possible for the planar heme but much more restricted when $Q_P > 0$, the activation entropy may be much more negative for an out-of-plane geometry. In the limiting case that rotation is not possible for the out-of-plane heme, the rotational molar entropy difference could be as large as $\Delta\Delta S^\ddagger = -(R/2)[1 + \ln(8\pi^2 I k_B T/h^2)] \approx -205 \text{ J/mol}\cdot\text{K}$ for each rotational degree of freedom. From these considerations, the entropy differences shown in Table 6 could arise from restrictions on CO ligand trajectories in the transition state for out-of-plane geometries of the heme iron. Figure 2 shows the location of the crossing point, and hence the activation entropy (ΔS^\ddagger) and enthalpy (ΔH^\ddagger) depend on Q_P . Clearly, the protein will play a role in determining where the transition state is located in Q_D , Q_P space.

The activation enthalpy $\Delta H^\ddagger(Q_P, Q_D)$ is maximal along the Q_P coordinate at the optimal out-of-plane geometry shown in Figure 1. The calculated optimal out-of-plane geometry shown in Figure 4 is $Q_{\text{deoxy}} \approx 0.25 \text{ \AA}$ and the value observed in many X-ray crystal structures is $Q_{\text{deoxy}} \approx 0.4 \text{ \AA}$. The magnitude $\Delta H^\ddagger(Q_P, Q_D)$ will be zero along Q_D until $Q_P > 0.2 \text{ \AA}$, at which point $\Delta H^\ddagger(Q_P, Q_D)$ along Q_D increases rapidly as Q_P increases (see Figure 2). The smallest barrier occurs for motion along the out-of-plane coordinate Q_P . Figure 4 shows that the barrier could be as large as $\approx 20 \text{ kJ/mol}$ if the transition state required iron motion into the plane of the heme iron. However, the calculations show that the barrier along Q_D drops to zero about halfway between the optimum Q_P geometry in the deoxy state and the in-plane geometry (see Figure 2C). Thus, the barrier can be smaller than 20 kJ/mol when the transition state occurs for an out-of-plane heme iron, $Q_P > 0$. On the other hand, the magnitude of the barrier could be larger because of electrostatic or steric interactions of the protein with the proximal ligand resulting in extra energy requirements to move along Q_P to minimize Q_D . The binding energy of ligands in the proximal pocket is -16 , -18 , and -19 kJ/mol for 1-Me Im, Im, and 4-Me Im, respectively.⁷⁷ In summary, steric differences that affect motion along the calculated PESs provide an explanation for the difference in activation enthalpy and entropy to rebinding for different proximal adducts.

Apparently, an inverse proportionality between the activation enthalpy and entropy is consistent with a variable crossing point along Q_P . The proximal adducts require different degrees of in-plane motion to reach a transition state. The crossing point Q_C will occur at different positions along Q_D since this coordinate is coupled to Q_P (Figure 2). When Q_C is located near the deoxy state, then ΔH^\ddagger is small and ΔS^\ddagger is large in magnitude and negative. If Q_C is located near the in-plane CO state, then ΔH^\ddagger is large and ΔS^\ddagger is smaller in magnitude and negative. The absolute value of ΔS^\ddagger depends on the effective concentration of the ligand in transition-state theory or the L-Z prefactor. Nonetheless, it appears that non-native ligands such as 1-Me Im and 4-Br Im require greater motion to reach the transition state (Q_C is nearer to an in-plane geometry) than 4-Me Im (Q_C is nearer to Q_{deoxy}). This may arise because of the $\approx 3 \text{ kJ/mol}$ greater stabilization of 4-Me Im in the proximal pocket.^{77,78} For example, even though 1-Me Im and 4-Me Im have nearly identical conformations as determined by X-ray crystallography, only 4-Me Im can form a hydrogen bond in the proximal pocket. While 4-Br Im may be able to form a hydrogen bond, it is likely much weaker and the bromine atom may not be as stabilizing as a methyl group in the hydrophobic proximal pocket. In other

words, the lack of stability of ligands such as 1-Me Im and 4-Br Im may permit them to move closer to the heme iron.

Conclusion

The kinetic data presented here show that ligand escape and protein relaxation are not strongly affected by proximal ligation of the heme iron. A detailed look at ligand escape shows that the activation parameters are weakly dependent on the identity of the proximal ligand. Thus, subtle effects are transmitted through the protein to the regions that are important for the exit of CO from the globin. The effect of proximal ligation on the kinetics of rebinding and on the free energy of binding is substantial. The escape equilibria, $K_{\text{escape}} = k_{23}/k_{32}$, and equilibria for CO rebinding, $K_{\text{CO}} = k_{21}/k_{12}$, vary by factors of ≈ 1.2 and ≈ 18 for the series of proximal ligands L considered here. The effect on the kinetics are similar with the effects on the inner process of CO rebinding that are 1 order of magnitude larger than those observed for CO escape. The data analysis complements an earlier study of protein relaxation studied by the Soret band shift.²⁸ That study showed that the protein relaxation observed in many time-resolved studies is not dependent on the iron coordinate but rather on distal side conformational changes such as reorientation of side chains as the CO ligand is trapped in the docking site.^{3,28} This result is intuitively appealing given the large number of time-resolved and cryogenically trapped X-ray structures that show significant displacement of distal residues around photolyzed CO in a docking site.^{58,79} Moreover, the idea that ligand escape is strongly affected by distal mutants but not by proximal conformations agrees with longstanding hypotheses regarding the importance of distal pathways for CO ligand escape in both hemoglobin and myoglobin.^{14,80–83} The model for the diatomic ligand recombination rate constant proposed has applicability to a wide range of heme proteins where CO and NO are probes of dynamic structure.

Acknowledgment. This work was supported by NSF grant MCB-9874895. S.F. gratefully acknowledges the North Carolina Supercomputer Center for support. Many thanks to Lee Bartolotti of the NCSC for advice and assistance. The kinetic measurements were performed in the laboratory of S. G. Boxer at Stanford University. The author thanks Dr. G. DePillis for assistance with the room temperature kinetic data.

Supporting Information Available: Information on the basis set, comparison of calculations using canonical and grand canonical ensemble are presented. Derivation of the four state kinetic model in the steady state approximation is given. This material is available free of charge via the Internet at <http://pubs.acs.org>.

References and Notes

- Balasubramanian, S.; Lambright, D. G.; Boxer, S. G. *Proc. Natl. Acad. Sci.* **1993**, *90*, 4718–4722.
- Balasubramanian, S.; Lambright, D. G.; Marden, M. C.; Boxer, S. G. *Biochemistry* **1993**, *32*, 2.
- Lambright, D. G.; Balasubramanian, S.; Boxer, S. G. *Biochemistry* **1993**, *32*, 10116–10124.
- Petrich, J. W.; Lambry, J. C.; Balasubramanian, S.; Lambright, D. G.; Boxer, S. G.; Martin, J. L. *J. Mol. Biol.* **1994**, *238*, 437–444.
- Nakashima, S.; Kitagawa, T.; Olson, J. S. *Chem. Phys.* **1998**, *226*, 323–336.
- Carver, T. E.; Rohlfis, R. J.; Olson, J. S.; Gibson, Q. H.; al., e. *J. Biol. Chem.* **1990**, *265*, 20007–20020.
- Hirota, S.; Li, T. S.; Phillips, G. N.; Olson, J. S.; Mukai, M.; Kitagawa, T. *J. Am. Chem. Soc.* **1996**, *118*, 7845–7846.

- (8) Scott, E. E.; Gibson, Q. H.; Olson, J. S. *J. Biol. Chem.* **2001**, 276, 5177–5188.
- (9) Smerdon, S. J.; Krzywdka, S.; Wilkinson, A. J.; R. E. Brantley, J.; Vaarver, T. E.; Hargrove, M. S.; Olson, J. S. *Biochemistry* **1993**, 32, 5132–5138.
- (10) Rohlf, R. J.; Mathews, A. J.; Carver, T. E.; Olson, J. S.; Springer, B. A.; Egeberg, K. D.; Sligar, S. G. *J. Biol. Chem.* **1990**, 265, 3168–3176.
- (11) Olson, J. S.; Phillips, G. N., Jr. *J. Biol. Inorg. Chem.* **1997**, 2, 544–552.
- (12) Olson, J. S.; Phillips, G. N. *J. Biol. Chem.* **1996**, 271, 17593–17596.
- (13) Lai, H. H.; Li, T.; Lyons, D. S.; Phillips, G. N., Jr.; Olson, J. S.; Gibson, Q. H. *Proteins* **1995**, 22, 322.
- (14) Ikedasaito, M.; Dou, Y.; Yonetani, T.; Olson, J. S.; al., e. *J. Biol. Chem.* **1993**, 268, 6855–6857.
- (15) Barrick, D. *Biochemistry* **1994**, 33, 6546–6554.
- (16) DePillis, G.; Decatur, S. M.; Barrick, D.; Boxer, S. G. *J. Am. Chem. Soc.* **1994**, 116, 6981–6982.
- (17) Decatur, S.; DePillis, G. D.; Boxer, S. G. *Biochemistry* **1996**, 35, 3925–3932.
- (18) Barrick, D.; Dahlquist, F. W. *Proteins Struct. Func. Genetics* **2000**, 39, 278–290.
- (19) Barrick, D. *Proteins: Struct., Funct., Genet.* **2000**, 39, 291–308.
- (20) Henry, E. R.; Sommer, J. H.; Hofrichter, J.; Eaton, W. A. *J. Mol. Biol.* **1983**, 166, 443–451.
- (21) Thorsteinsson, M. V.; Kerby, R. L.; Roberts, G. P. *Biochemistry* **2000**, 39, 8284–8290.
- (22) Negrier, M.; Berka, V.; Vos, M. H.; Liebl, U.; Lambry, J. C.; Tsai, A. L.; Martin, J. L. *J. Biol. Chem.* **1999**, 274, 24694–24702.
- (23) Stone, J. R.; Marletta, M. A. *Biochemistry* **1996**, 35, 1093–1099.
- (24) Petrich, J. W.; Poyart, C.; Martin, J. L. *Biochemistry* **1988**, 27, 4049–4060.
- (25) Franzen, S.; Bohn, B.; Poyart, C.; DePillis, G.; Boxer, S. G.; Martin, J. L. *J. Biol. Chem.* **1995**, 270, 1718–1720.
- (26) Franzen, S.; Kiger, L.; Poyart, C.; Martin, J. L. *Biophys. J.* **2001**, 80, 2372–2385.
- (27) Cao, W. X.; Sjodin, T.; Sage, J. T.; Ye, X.; Demidov, A. A.; Wang, W.; Champion, P. M.; Barrick, D. *Biophys. J.* **2001**, 80, 1164.
- (28) Franzen, S.; Boxer, S. G. *J. Biol. Chem.* **1997**, 272, 9655–9660.
- (29) Tian, W. D.; Sage, J. T.; Srajer, V.; Champion, P. M. *Phys. Rev. Lett.* **1992**, 68, 408–411.
- (30) Lim, M.; Jackson, T. A.; Anfinrud, P. A. *Proc. Natl. Acad. Sci. U.S.A.* **1993**, 90, 5801–5804.
- (31) Jackson, T. A.; Lim, M.; Anfinrud, P. A. *Chem. Phys.* **1994**, 180, 131–140.
- (32) Lim, M. H.; Jackson, T. A.; Anfinrud, P. A. *Nat. Struct. Biol.* **1997**, 4, 209–214.
- (33) Lambright, D. G.; Balasubramanian, S.; Boxer, S. G. *Chem. Phys.* **1991**, 158, 249–260.
- (34) Ansari, A.; Berendzen, J.; Braunstein, D.; Cowen, B. R.; Frauenfelder, H.; Hong, M. K.; Iben, I. E. T.; Johnson, J. B.; Ormos, P.; Sauke, T. B.; Scholl, R.; Schulte, A.; Steinbach, P. J.; Vittitow, J.; Young, R. D. *Biophys. Chem.* **1987**, 26, 337–355.
- (35) Ansari, A.; Jones, C. M.; Henry, E. R.; Hofrichter, J.; Eaton, W. A. *Biochemistry* **1994**, 33, 5128–5145.
- (36) Steinbach, P. J.; Ansari, A.; Berendzen, J.; Braunstein, D.; Chu, K.; Cowen, B. R.; Ehrenstein, D.; Frauenfelder, H.; Johnson, J. B.; Lamb, D. C.; Luck, S.; Mourant, J. R.; Nienhaus, G. U.; Ormos, P.; Philipp, R.; Xie, A.; Young, R. D. *Biochemistry* **1991**, 30, 3988–4001.
- (37) Findsen, E. W.; Friedman, J. M.; Ondrias, M. R. *Biochemistry* **1988**, 27, 8719–8724.
- (38) Srajer, V.; Reinisch, L.; Champion, P. M. *J. Am. Chem. Soc.* **1988**, 110, 6656–6670.
- (39) Srajer, V.; Champion, P. M. *Biochemistry* **1991**, 30, 7390–7402.
- (40) Tian, W. D.; Sage, J. T.; Champion, P. M.; Chien, E.; Sligar, S. G. *Biochemistry* **1996**, 35, 3487–3502.
- (41) Tian, W. D.; Sage, J. T.; Champion, P. M. *J. Mol. Biol.* **1993**, 233, 155–166.
- (42) Franzen, S.; Lambry, J. C.; Bohn, B.; Poyart, C.; Martin, J. L. *Nat. Struct. Biol.* **1994**, 1, 230–233.
- (43) Franzen, S.; Bohn, B.; Poyart, C.; Martin, J. L. *Biochemistry* **1995**, 34, 1224–1237.
- (44) McMahon, B. H.; Stojkovic, B. P.; Hay, P. J.; Martin, R. L.; Garcia, A. E. *J. Chem. Phys.* **2000**, 113, 6831–6850.
- (45) DeVault, D. *Quantum-Mechanical Tunneling in Biological Systems*; Cambridge University Press: Cambridge, 1984.
- (46) Vogel, K. M.; Kozlowski, P. M.; Zgierski, M. Z.; Spiro, T. G. *1999*, 121, 9915–9921.
- (47) Vogel, K. M.; Kozlowski, P. M.; Zgierski, M. Z.; Spiro, T. G. *Inorg. Chim. Acta* **2000**, 297, 11–17.
- (48) Ghosh, A.; Bocian, D. F. *J. Phys. Chem.* **1996**, 100, 6363–6367.
- (49) Rovira, C.; Parrinello, M. *Biophys. J.* **2000**, 78, 93–100.
- (50) Rovira, C.; Kunc, K.; Hutter, J.; Ballone, P.; Parrinello, M. *J. Phys. Chem. A* **1997**, 101, 8914–8925.
- (51) Harvey, J. N. *J. Am. Chem. Soc.* **2000**, 122, 12401–12402.
- (52) Franzen, S. *J. Am. Chem. Soc.*, in press.
- (53) Agmon, N.; Hopfield, J. J. *J. Chem. Phys.* **1983**, 79, 2042–2053.
- (54) Peterson, E.; Chien, E.; Sligar, S.; Friedman, J. *Biochemistry* **1998**, 37, 12301–12319.
- (55) Huang, X. H.; Boxer, S. G. *Nat. Struct. Biol.* **1994**, 1, 34–37.
- (56) Hofrichter, J.; Sommer, J. H.; Henry, E. R.; Eaton, W. A. *Proc. Natl. Acad. Sci. U.S.A.* **1983**, 80, 2235–2239.
- (57) Austin, R. H.; Beeson, K. W.; Eisenstein, L.; Frauenfelder, H.; Gunsalus, I. C. *Biochemistry* **1975**, 14, 5355–5373.
- (58) Schlichting, I.; Berendzen, J.; Phillips, G. N., Jr.; Sweet, R. M. *Nature* **1994**, 371, 808–812.
- (59) Engler, N.; Ostermann, A.; Gassmann, A.; Lamb, D. C.; Prusakov, V. E.; Schott, J.; Schweitzer-Stenner, R.; Parak, F. G. *Biophys. J.* **2000**, 78, 2081–2092.
- (60) Melchers, B.; Knapp, E. W.; Parak, F.; Cordone, L.; Cupane, A.; Leone, M. *Biophys. J.* **1996**, 70, 2092–2099.
- (61) Srajer, V.; Teng, T. Y.; Ursby, T.; Pradervand, C.; Ren, Z.; Adachi, S.; Schildkamp, W.; Bourgeois, D.; Wulff, M.; Moffat, K. *Science* **1996**, 274, 1726–1729.
- (62) Teng, T.-Y.; Srajer, V.; Moffat, K. *Nat. Struct. Biol.* **1994**, 1, 701–705.
- (63) Franzen, S.; Shreve, A. P.; Wallace-Williams, S. E.; Dyer, R. B. *J. Phys. Chem. B* **2000**, 103, 7969–7975.
- (64) Hagen, S. J.; Eaton, W. A. *J. Chem. Phys.* **1996**, 104, 3395–3398.
- (65) Hagen, S. J.; Hofrichter, J.; Eaton, W. A. *Science* **1995**, 269, 959–962.
- (66) Franzen, S. *Chem. Phys.*, submitted for publication.
- (67) Kohlrausch, R. *Ann. Phys.* **1847**, 12, 392.
- (68) Perdev, J. P.; Chevray, J. A.; Vosko, S. H.; Jackson, K. A.; Pederson, M. R.; Singh, D. J.; Fiolhais, C. *Phys. Rev. B* **1992**, 46, 6671–6687.
- (69) Becke, A. D. *J. Chem. Phys.* **1997**, 107, 8554–8560.
- (70) Lee, C. L.; Yang, W.; Parr, R. G. *Phys. Rev. B.* **1988**, 37, 785–789.
- (71) Delley, B. *J. Chem. Phys.* **1990**, 92, 508–517.
- (72) Delley, B. *J. Chem. Phys.* **2000**, 113, 7756–7764.
- (73) Bartolotti, L. Personal communication, 2001.
- (74) Kohn, W.; Sham, L. J. *Phys. Rev. A* **1965**, 137, 1697–1699.
- (75) Mermin, D. *Phys. Rev. A* **1965**, 137, 1441–1443.
- (76) Hofman, K. *Imidazole and Its Derivatives, Part I*; Interscience Publishers: New York, 1953.
- (77) Decatur, S. M.; Franzen, S.; DePillis, G. D.; Dyer, R. B.; Woodruff, W. H.; Boxer, S. G. *Biochemistry* **1996**, 35, 4939–4944.
- (78) Decatur, S. M.; Belcher, K. L.; Rickert, P. K.; Franzen, S.; Boxer, S. G. *Biochemistry* **1999**, 38, 11086–11092.
- (79) Vojtechovsky, J.; Chu, K.; Sweet, R. M.; Berendzen, J.; Schlichting, I. *Biophys. J.* **1999**, 77, 2153–2174.
- (80) Scott, T. W.; Friedman, J. M.; Macdonald, V. W. *J. Am. Chem. Soc.* **1985**, 107, 3702–3705.
- (81) Ramsden, J.; Spiro, T. G. *Biochemistry* **1989**, 28, 3125–3128.
- (82) Quillin, M. L.; Arduini, R. M.; Olson, J. S.; Phillips, G. N. *J. Mol. Biol.* **1993**, 234, 140–155.
- (83) Perutz, M. F. *Annu. Rev. Biochem.* **1979**, 48, 327–386.